Origins versus fingerprints of the Jahn-Teller effect in d-electron ABX_3 perovskites

Julien Varignon,[1,2] Manuel Bibes,[1] and Alex Zunger[3]
[1]*Unité Mixte de Physique, CNRS, Thales, Université Paris Sud, Université Paris-Saclay, F-91767 Palaiseau, France*
[2]*Laboratoire CRISMAT, CNRS UMR 6508, ENSICAEN, Normandie Université, 6 boulevard Maréchal Juin, F-14050 Caen Cedex 4, France*
[3]*Energy Institute, University of Colorado, Boulder, Colorado 80309, USA*

(Received 18 June 2019; published 26 November 2019)

The Jahn-Teller distortion that can remove electronic degeneracies in partially occupied states and results in systematic atomic displacements is a common underlying feature to many of the intriguing phenomena observed in 3d perovskites, encompassing magnetism, superconductivity, orbital ordering, and colossal magnetoresistance. Although the seminal Jahn and Teller theorem was postulated almost a century ago, the origins of this effect in perovskite materials are still debated, including propositions such as superexchange, spin-phonon coupling, sterically induced lattice distortions, and strong dynamical correlation effects. Although the end result of Jahn-Teller distortions often includes a mix of such various contributions, due to coupling of various lattice, spin, and electronic modes with the distortions ("fingerprints" or "consequences" of Jahn-Teller), it is not clear what the primary cause is, i.e., which cases are caused by a pure electronic instability associated with degeneracy removal, as implied in the Jahn-Teller theorem, and which cases originate from other causes, such as semiclassical size effects. We propose a way to distinguish the materials with an electronic instability associated with degeneracy removal being the primary cause of the Jahn-Teller distortions, from others with octahedral rotation or tilts from a steric effect playing the primary role in electron-lattice coupling. This work provides a unified and quantitative density functional theory explanation of the experimentally observed trends of octahedral deformations in ABX_3 perovskites, without recourse to the dynamically correlated vision of electron interactions codified by the Mott-Hubbard mechanism. We inquire about the origin and predictability of different types of octahedral deformation by using a Landau-esque approach, where the orbital occupation pattern of a symmetric structure is perturbed, finding whether it is prone to total energy lowering the electronic instability or not. This is done for a systematic series of ABX_3 perovskite compounds having 3d-orbital degeneracies, using the density functional approach. We identify (i) systems prone to an electronic instability (a true Jahn-Teller effect), such as $KCrF_3$, $KCuF_3$, $LaVO_3$, $KFeF_3$, and $KCoF_3$, where the instability is independent of magnetic order, and forces a specific orbital arrangement that is accommodated by a BX_6 octahedral deformation with a specific symmetry. On the other hand, (ii) compounds such as $LaTiO_3$ and $LaMnO_3$ with delocalized d states do not show any electronically driven instability. Here, the alternate orbital ordering, which is an energy-lowering event irrespective of the presence of electronic instabilities, simply results from the coupling of lattice modes induced by semiclassical size effects (sterically induced), such as BX_6 octahedra rotations. (iii) Although RVO_3 (R = Lu-La, Y) perovskites exhibit hybridizations similarly to $LaTiO_3$, their t_{2g}^2 electronic structure is highly unstable and preserves the Jahn-Teller effect. However, here coexisting steric deformations and Jahn-Teller distortions result in strongly entangled spin-orbital properties.

DOI: 10.1103/PhysRevResearch.1.033131

I. INTRODUCTION

ABX_3 (X = O, F) perovskites [1,2] show a number of systematic atomic distortions relative to the ideal cubic perovskite structure made of corner-sharing, vertically positioned, all-parallel BX_6 octahedra with equal B-X bonds. The interpretation of much of the electronic and magnetic phenomenology surrounding such perovskites [1,2], including superconductivity, colossal magnetoresistance, orbital ordering, and metal-insulator transitions is intimately related to the understanding of the causes versus consequences of the observed atomic distortions. The causes of such distortions in the specific case of Mott insulators are related to the broader issue of causes of gap formations in such compounds. In the electron correlation literature [3–5], gapping in Mott insulators has been directly related to interelectronic repulsion U in the symmetric, undistorted state, leading to the expectation that such gapping is a many-body correlation effect. Distortions can occur later as an independent effect. Recent literature predicting distortions in $LaMnO_3$ using dynamically correlated approaches [3] specifically attributed the causes of such distortions to dynamic correlations. Indeed, previous work claimed that the local density approximation (LDA) and generalized gradient approximation (GGA) "usually fail to predict the correct electronic and structural properties of

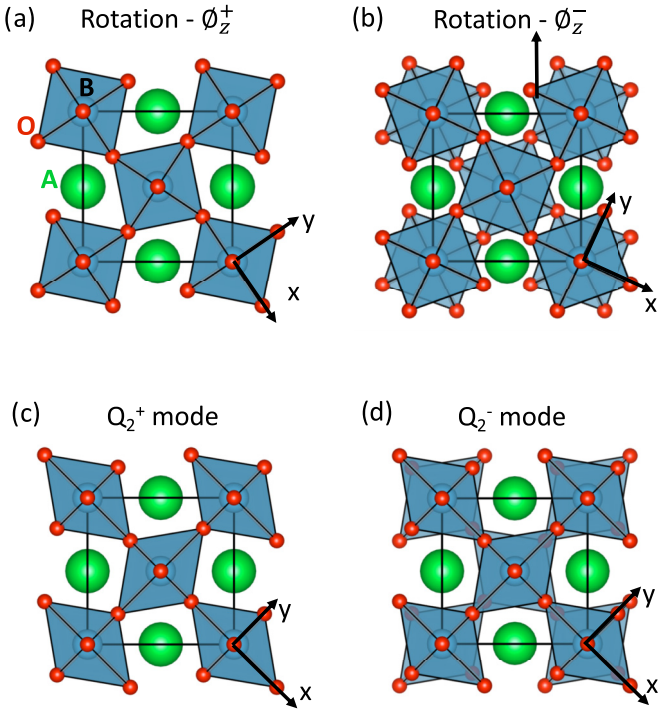

FIG. 1. Sketches of the key lattice distortions appearing in ABX_3 materials. (a) and (b) In-phase [ϕ_z^+, (a)] and antiphase [ϕ_z^-, (b)] octahedral rotations around the z axis. (c) and (d) Octahedral deformations propagating in phase [Q_2^+, (c)] or in antiphase [Q_2^-, (d)] along the z axis.

materials where electronic correlations play a role" [9]; similar statements abound in the literature [3,5,6]. Nevertheless, such a belief was often grounded on a naive implementation of density functional theory (DFT) using non-spin-polarized simulations and/or a lack of symmetry-breaking modes and the use of simple exchange-correlation functionals that do not distinguish occupied from unoccupied orbitals. Recent works [7–10] have clarified the fact that strong dynamical correlations need not be the determining factor for gap opening or symmetry-lowering displacements in ABO_3 materials. Instead, gapping in oxide Mott insulators can be a consequence of symmetry breaking (positional, occupational, moment distribution) and can be obtained in single-determinant mean-field-like DFT calculations even at $U = 0$ eV [7,11]. Using U in DFT calculations is not the same as using U in a Hubbard Hamiltonian; in the former case U helps to reduce self-interaction error thereby making orbitals spatially more compact and thereby increasing the gain in energy from electronic degeneracy removal, thus better competing with energy cost from the atomic distortions. This realization suggests taking a new look at the causes and consequences of distortions in Mott insulators and related compounds.

Usually, distortion in ABX_3 perovskites produces inequivalent B-X bond lengths, such as the Q_2 motion (cf. Fig. 2 of Ref. [12]) that differentiates bond lengths along the x and y directions. This exists either as in-phase motion in consecutive planes along the z axis [here labeled Q_2^+ motion; Fig. 1(c)] or as in antiphase along z [here labeled Q_2^- motion; Fig. 1(c)]. Although octahedral deformation tilts [e.g., the in-phase ϕ_z^+ and antiphase ϕ_z^-; displayed in Figs. 1(a), 1(b)] in different ABX_3 compounds often appear similar, they might have different origins. Possibilities include being (i) a consequence of the classic size mismatch between the A, B, and X atoms, as reflected by geometrical packing constructs such as the Goldschmidt tolerance factor [13], or (ii) a true Jahn-Teller [1,6,12,14] effect (JTE), reflecting an electronic instability associated with partial occupation of degenerate states, as described in the seminal work of Jahn and Teller [15]. Understanding predictively the causes of the observed displacements is central to interpreting numerous related phenomena, e.g., gap formation due to symmetry lowering, metal-insulator transitions [16], orbital orderings [5,17,18], and magnetic interactions [19] in ABX_3 perovskites. This is important since controlling octahedral deformations by using temperature, ferroelectricity, strain engineering, or heterostructures [20–27] may offer much needed knobs to control electronic devices.

Puzzles. Predictive understanding of the mechanisms of octahedral distortions is rather challenging, for a number of reasons:

(a) Compounds with the same degenerate electronic configurations such as $KCrF_3$ [28], $KCuF_3$ [29], and $LaMnO_3$ [30] all being e_g^1 or YVO_3 and $LaVO_3$ both being t_{2g}^2 [31] show different types of octahedral deformations at low temperature—Q_2^- for $KCrF_3$, $KCuF_3$, or $LaVO_3$ and Q_2^+ for YVO_3 and $LaMnO_3$—raising the question of what creates Q_2^+ and what creates Q_2^-.

(b) Recent theoretical works predicted the surprising appearance of strong in-phase Q_2^+ symmetry-lowering octahedral deformations in compounds such as $SrTiO_3$, $BaMnO_3$, or $BiFeO_3$ even when there are no degenerate states (t_{2g}^0, t_{2g}^3, or $t_{2g}^3e_g^2$ configurations, respectively) [22,32].

(c) The textbook depiction of the Jahn-Teller force is often based on calculations based on the degenerate orbital alone, but one must consider the force resulting from the system's total energy, including not only the sum of one-electron orbital energy but also the electron-electron Coulomb and exchange-correlation energies resulting from degeneracy removal.

Literature models for explaining the origin of octahedral deformations in ABX_3 materials span a large range of mechanisms, including electronic superexchange as codified by the Kugel-Khomskii model [18,19], electron-phonon coupling [5,33], lattice mode couplings involving rotations and forcing the Q_2^+ mode [21,34,35], or specific dynamical correlation effects [3,6]. The Kugel-Khomskii approach represents a phenomenological approach to understanding the connection between orbital and spin order. However, it does not identify electronic and structural origins of what is a Jahn-Teller effect in perovskites, since both Q_2^+ and Q_2^- modes are equally assumed to be Jahn-Teller distortions.

Since none of these existing models or visions to explain Jahn-Teller distortions have been applied to a full range of ABX_3 compounds with different e_g-like and t_{2g}-like orbital occupations, at this time it is not clear whether different mechanisms are needed to explain different distortions in different compounds, whether Q_2^+ and Q_2^- modes really reflect Jahn-Teller effects, and whether there is a basic theoretical framework that could explain them all.

Distinguishing features of the current approach. We address this subject by studying several ABX_3 materials (X = O, F) with a transition-metal element exhibiting degenerate states (but without a propensity to undergo the disproportionation effect) using a mean-field-like Bloch-periodic DFT band theory with two stipulations. First, a polymorphous representation of the real-space structure that permits the existence of different local environments to atoms and spins is required. This entails using crystallographic cells that are not limited to the smallest primitive cell and therefore allow orbital, spatial, and spin symmetry breaking, should these modes lower the total energy. Second, breaking orbital symmetries of degenerate partners requires an exchange correlation functional that distinguishes occupied from unoccupied states, thereby affording significant cancellation of the self-interaction error and thus spatial compactness of $3d$ orbitals. Here we use DFT + U (but nonzero U is not essential, as other exchange correlation functionals make no use of an explicit U term [7]). This approach provides DFT with a fair opportunity to reveal whether the different patterns of symmetry breaking—spin order, Jahn-Teller distortion and/or octahedral rotations, and orbital occupation symmetry breaking—lower the energy or not, thereby establishing a first-principles framework for predictive theory of displacements in ABX_3 perovskites.

A Landau-esque perturbation approach. To determine whether a potential deformation has an electronic origin or not we use a Landau-esque perturbation approach that examines whether symmetry lowering via nudged occupation numbers in a degenerate manifold of an initially high-symmetry cubic cell lowers the total energy or not. We examine the total energy for a number of prototypical cases encountered in $3d$ ABX_3 compounds: (a) the equal-occupation scenario of a degenerate level [such as (1/2, 1/2) for a single electron in a doubly occupied e_g level] and (b) the orbital broken symmetry (OBS) scenario of degenerate partners, e.g., (1, 0). If (b) gives total energy lowering relative to (a) this signals the propensity for an electronic instability in the parent high-symmetry phase, which is then followed up by the complete relaxation of the unit cell displacements, providing our predicted Jahn-Teller distortions (possibly with coupling to octahedral tilting). If the unequal-occupation configuration (b) returns to the equal-occupation configuration (a) during self-consistent calculation, this indicates that the high-symmetry system is electronically stable and thus not prone to develop an *electronically enforced* Jahn-Teller distortion. Distortions present may reflect other factors such as the classic steric effects induced by size mismatch.

The main conclusions are as follows:

(a) The existence of electronic instabilities, i.e., a true JTE, is predicted in the high-symmetry $Pm\bar{3}m$ cubic phase of several ABX_3 compounds ($KCrF_3$, $KCuF_3$, $LaVO_3$, $KFeF_3$, and $KCoF_3$), whereas $LaMnO_3$ or $LaTiO_3$ have no such instability. Instabilities are manifested by the breaking of orbital degeneracies while lowering the total energy, and thereby concomitantly opening finite band gaps.

(b) Orbital ordering is always found to be a total-energy-lowering event. In such a state, electrons occupy an orbital that is pointing toward orthogonal directions between all nearest-neighbor $3d$ atoms, such as alternation of d_{xy}/d_{yz} orbitals for a material with a t_{2g} degeneracy or alternation of d_{y^2}/d_{x^2} orbitals for a material with an e_g-level degeneracy, thereby minimizing orbital interactions as codified by the phenomenological electronic superexchange model of Kugel and Khomskii. The above observations are independent of the imposed magnetic ordering, thus substantiating the view that the magnetic order is not the cause of the Jahn-Teller effect and related orbital ordering, but rather a consequence of these phenomena.

(c) The Q_2^- octahedral deformation mode is a Jahn-Teller distortion: Following the identification of electronic instabilities in cubic cells, we follow the quantum mechanical forces to establish the fully relaxed crystal structures, finding that the aforementioned Jahn-Teller distorted compounds develop a Q_2^- octahedra deformation mode, which is therefore identified as an electronically induced Jahn-Teller distortion. The significance of the development of this specific Q_2^- mode is that it is characterized by *opposite* octahedral deformations between nearest sites and is thus able to accommodate the electronically induced orbital ordering. Calculation of the magnitude of the displacements shows good agreement with the experimentally observed trends in a full range of ABX_3 compounds with t_{2g} and e_g degenerate partners.

(d) At odds with the common perception, $LaMnO_3$ does not exhibit JTE whereas $KCrF_3$ does, despite isovalent ($t_{2g}^3 e_g^1$) configurations. Similarly, the t_{2g}^1 configuration $LaTiO_3$ has no Jahn-Teller distortion, whereas $KFeF_3$ does. This is because the existence of strong hybridization in the oxide cases diminishes the orbital localization needed to create the Jahn-Teller distortion, whereas in the fluoride the hybridization is much weaker.

(e) The Q_2^+ octahedral deformation, appearing in $LaMnO_3$ or $LaTiO_3$, is not induced by an electronic instability and thus it is not a Jahn-Teller distortion. It is a consequence of octahedral rotations and tilts often appearing in the perovskite oxides due to pure semiclassical atomic size effects, i.e., geometric steric effects. The Q_2^+ octahedral deformation mode thus cannot signal strong dynamical correlation effects in these ABX_3 compounds.

(f) Although $LaVO_3$ exhibits B d–X p hybridizations similarly to $LaTiO_3$, the former compound exhibits a robust electronic instability in the cubic cell while $LaTiO_3$ has zero stabilization energy. The reason is that $LaVO_3$ has two electrons, t_{2g}^2, relative to $LaTiO_3$ with just one, t_{2g}^1.

(g) Due to the coexistence of a JTE and of octahedral rotations in RVO_3 materials, the Q_2^- and Q_2^+ modes compete and result in two distinct spin-orbital orders at low temperature depending on the octahedral rotation amplitude.

(h) Jahn-Teller distortions as well as semiclassical size effect distortions can contribute to the opening of band gaps in Mott insulators. We have previously identified [10] four gapping modalities; the JTE contributes just to modality (iii) as follows: (i) compounds with closed subshells that can open a gap due to octahedral crystal field splitting ($CaMnO_3$, $LaFeO_3$), (ii) compounds opening gaps by lifting degeneracies through large symmetry-lowering displacements such as X_6 rotations ($LaTiO_3$ or $LaMnO_3$), (iii) compounds with two electrons in t_{2g} levels exhibiting Jahn-Teller-induced electronic instability able to cause gapping such as $LaVO_3$ ($t_{2g}^2 e_g^0$), and (iv) compounds with unstable single local electronic occupation patterns disproportionating into a double local environment, e.g., $CaFeO_3$ and $YNiO_3$.

We conclude that the electronically induced Jahn-Teller distortion mode Q_2^- and the geometrically induced steric Q_2^+ octahedral deformation mode are fully captured by a static mean-field method. This is in line with recent theoretical works that have demonstrated that static mean-field methods capable of inducing broken symmetry such as density functional theory [7,10,21,34] in a polymorphous representation suffice to also explain (i) the trends in gapping and type of magnetic order across the ternary ABO_3 series [10] and the binary $3d$ oxide series [8,36]; (ii) the trends in disproportionation into two different local environments of the B site $2ABO_3 \rightarrow A_2[B, B']O_6$ [9]; and (iii) the explanation of doping Mott insulators including cuprates [37,38], doping kagome structures [39], as well as "antidoping" oxides [40].

II. THE ELEMENTS OF THE METHOD

The main features of the theoretical framework used in the study are as follows:

(a) *Cell geometry and relaxation*. We consider the following structure types: a high-symmetry $Pm\bar{3}m$ cubic cell ($LaTiO_3$, $LaVO_3$, $LaMnO_3$, $KFeF_3$, $KCoF_3$, $KCrF_3$, and $KCuF_3$) as well as the experimentally observed structures, namely I_4/mcm ($KCuF_3$, $KCrF_3$), $Pbnm$ ($LaTiO_3$, $LaVO_3$, $LaMnO_3$, $LaTiO_3$), $P2_1/b$ ($LaVO_3$), I_2/m ($KCrF_3$), $P\bar{1}$ ($KCoF_3$), and I_2/a ($KFeF_3$), for identifying the DFT ground state structure. We allow cell sizes larger than the minimal one (one formula unit per cell) so as to permit symmetry-breaking distortions, should they lower the total energy. Atoms have to be nudged initially off their high-symmetry positions in the cubic cell, followed by the calculation of the restoring Hellman-Feynman forces guiding full relaxation. In order to provide sufficient flexibility for developing general patterns of energy-lowering deformations we have used a polymorphous crystallographic cell corresponding to a $(\sqrt{2}a, \sqrt{2}a, 2a)$ cubic cell (i.e., 4 f.u. per cell). A polymorphous network [7,8,10] refers to cases where the macroscopically averaged symmetry (seen by XRD with intensities fitted to a minimal unit cell) is high while the local symmetries can be low. Polymorphous networks will generally show such distortions when positional and occupational degrees of freedom are nudged in a supercell calculation. In contrast, a monomorphous network refers to cases where a single structural motif exists, as seen in calculations that restrict the cell to a minimal size. The structural relaxation (lattice parameters and atomic positions) of ground state structures has also been performed until forces are lower than 0.5 meV/Å. We performed a symmetry-adapted mode analysis that allows us to extract the amplitudes of general distortion modes by projecting the distorted structure on the basis of the phonon eigendisplacements of the high-symmetry cubic cell [41,42].

(b) *Orbital symmetry breaking*. The occupation numbers of partially filled degenerate orbitals in the high-symmetry cubic cell are not restricted to equal occupations of the degenerate partners. For a compound with a single e_g electron, we do not preselect a (1/2, 1/2) occupation pattern as generally done in standard band calculations, but allow also exploration of a (1, 0) occupation pattern. Analogously, for 2 electrons in the t_{2g} level we explore (2/3, 2/3, 2/3) versus (1, 1, 0) occupation patterns. Wave function symmetrization to a presumed symmetry is avoided so as to allow electrons to freely occupy energy-lowering configurations. We therefore initially nudge not only atomic positions but also the occupation patterns of electrons in specific degenerate partners, called orbital broken symmetry (OBS) states [43–45]. The self-consistent field with possible changes in d-orbital occupancies is then obtained starting from this initial guess.

(c) *Spin order*. We use the observed low-temperature spin order, e.g., AFMA (ferromagnetic planes coupled antiferromagnetically together), AFMC (AFM planes coupled ferromagnetically together), and AFMG (all nearest-neighbor cations are antiferromagnetically coupled). Since we have previously shown that a low-temperature spin-ordered phase inherits the physics of the high-temperature paramagnetic (PM) phase in ABO_3 materials [10], we did not attempt to model the PM distortions presently. For the study of the linear response of the ideal cubic phase, we prefer to use a simple FM order so as to avoid potentially strongly entangled spin-orbital situations as codified by the Kugel-Khomskii model [18,19], i.e., the chicken and the egg dilemma. This is reinforced by experimental observations of octahedral deformations appearing at higher temperatures than the AFM to PM (for example, in $KCrF_3$, $KCuF_3$, $LaMnO_3$).

(d) *Exchange-correlation functional*. To enable energy-lowering occupations one needs to use an exchange-correlation (XC) functional that distinguishes occupied from unoccupied states. Local (LDA) and semilocal (GGA, meta-GGA) XC functionals do not make such a distinction. The simplest XC allowing this is DFT + U, where U is an on-site potential acting on a subset of orbitals—here the transition metal (TM) d states—and shifting to lower (upper) energies occupied (unoccupied) levels. We have thus employed this formalism in combination with the PBEsol [46] XC functional where U is an effective parameter $U_{\text{eff}} = U$-J [47]. We did not optimize the effective U values for each material to achieve an optimal fit (this might be done if needed in the future), but opted instead to use fixed $U = 3.5$ eV for all $3d$ TM elements for simplicity.

III. RESULTS

A. Examining the propensity of the symmetric structure for electronically induced distortions

The Landau-esque symmetry-breaking test perturbs a high-symmetry cubic cell (here, $Pm\bar{3}m$ with lattice parameter a_{cub} that is initially relaxed) and examines the total energy for (a) assumed equal occupations of the degenerate partners [no OBS, such as (1/2, 1/2) for a single electron in a doubly degenerate e_g level] and (b) OBS, looking for energy-lowering configurations [e.g., (1, 0)]. The spin configuration used is FM. Energy differences between these configurations are provided in Table I.

We see that given the opportunity for orbital broken symmetry, the compounds $LaVO_3$, $KFeF_3$, $KCoF_3$, $KCrF_3$, and $KCuF_3$ show an energy gain $\Delta E_{\text{OBS}-\text{no OBS}} < 0$, with a concomitant opening of the band gap, while $LaTiO_3$ and $LaMnO_3$ have $\Delta E_{\text{OBS}-\text{no OBS}} = 0$; i.e., the initially imposed OBS relaxes back to the configuration with equally occupied degenerate orbitals, and the system stays metallic. These

TABLE I. Detection of a spontaneous electronic instability in the high-symmetry cubic phase of ABX_3 perovskites. Energy differences between solutions with equal occupancy of degenerate levels (no OBS) and with the most stable OBS state in meV per formula unit obtained with GGA + U and HSE06 functionals (the latter uses a smaller cubic cell for computational cost reasons). The lattice parameter a is fixed to a relaxed cubic cell without OBS. A FM order is assumed. Results for the ground state AFM order are reported in parentheses, namely AFMG for $LaTiO_3$, $KFeF_3$, and $KCoF_3$; AFMC for $LaVO_3$; and AFMA for $LaMnO_3$, $KCrF_3$, and $KCuF_3$.

		$(\sqrt{2}a, \sqrt{2}a, 2a)$ cubic cell (GGA + U)		Primitive cubic cell (HSE06)
	Electronic configuration	$\Delta E_{\mathrm{OBS-no\,OBS}}$ (meV/f.u.)	E_g (eV)	$\Delta E_{\mathrm{OBS-no\,OBS}}$ (meV/f.u.)
$LaTiO_3$	d^1 $(t^1_{2g\uparrow})$	0 (0)	0	0
$LaMnO_3$	d^4 $(t^3_{2g\uparrow}e^1_{g\uparrow})$	0 (0)	0	0
$LaVO_3$	d^2 $(t^2_{2g\uparrow})$	−297 (−237)	0.42	−428
$KFeF_3$	d^6 $(t^3_{2g\uparrow}e^2_{g\uparrow}t^1_{2g\downarrow})$	−655 (−873)	1.78	−780
$KCoF_3$	d^7 $(t^3_{2g\uparrow}e^2_{g\uparrow}t^2_{2g\downarrow})$	−726 (−895)	1.90	−1071
$KCrF_3$	d^4 $(t^3_{2g\uparrow}e^1_{g\uparrow})$	−124 (−85)	0.66	−256
$KCuF_3$	d^9 $(t^3_{2g\uparrow}e^2_{g\uparrow}t^3_{2g\downarrow}e^1_{g\downarrow})$	−71 (−81)	0.38	−477

observations are unchanged by using another nonlocal functional such as the HSE06 [48,49] hybrid functional method, having also a good adherence to self-interaction cancellation (see the method section at the end of Sec. IV for the protocol we used to perform OBS studies with the HSE06 functional). It is significant that the sign of the energy difference is unaltered when one uses instead of the FM spin configuration the ground state magnetic order, namely AFMG for $LaTiO_3$, $KFeF_3$, and $KCoF_3$, AFMC for $LaVO_3$, and AFMA for $LaMnO_3$, $KCrF_3$, and $KCuF_3$; see numbers in parentheses in Table I. Finally, although VASP detects a D_{4h} instead of a O_h point group symmetry with the $(\sqrt{(2)}a, \sqrt{(2)}a, 2a)$ supercell that may weaken the Jahn-Teller force, we have checked that larger $(2a, 2a, 2a)$ supercells associated with the proper O_h point group symmetry still produce a total absence of electronic instabilities in $LaTiO_3$ and $LaMnO_3$.

1. The emergence of orbital order as a DFT total-energy-lowering Jahn-Teller effect

Once the degeneracies of the high-symmetry phase are removed, one notes the creation of deterministic localization patterns of the degenerate partner components (such as $d_{x^2-y^2}$ and d_{z^2}) on different atomic sites. This "orbital ordering" has intrigued the 3d oxide community [12,19], raising various exotic interpretations [3,6,18,19,21,33–35]. To understand the possible unexotic, mean-field total energy origins of such orbital ordering, we have investigated the energetics of different assumed orbital arrangements: (a) electrons in the degenerate levels are initially nudged in *identical* orbitals on all nearest transition metal sites, such as a d_{z^2} occupancy on all sites for a compound with a single e_g electron; (b) the electron is initially nudged in a *different* degenerate partner between nearest TM sites in the (xy) plane but on *the same* partner for TM located in the consecutive plane along the z direction, such as alternation of d_{x^2} and d_{y^2} in the xy plane with a similar arrangement on the consecutive plane along z, thus forming a "columnar arrangement"; and (c) the electron is initially nudged in a *different* degenerate partner between *all* nearest-neighbor sites, such as alternation of d_{x^2} and d_{y^2} in all Cartesian directions, thus forming a 3D checkerboard. For a compound with 2 unpaired electrons for t_{2g} levels, cases (b) and (c) necessarily require that an identical orbital has to be occupied between nearest TM sites. We thus imposed one electron in a specific t_{2g} partner on all TM sites (d_{xy} here) and then we alternate the occupancy of the remaining partners (d_{xz}/d_{yz}). After initial nudging (intended to avoid accidental local minimum), the solution is iterated to self-consistency with full relaxation of the electronic structure but without any structural relaxation.

The results show that for all compounds displaying a spontaneous electronic instability, the lowest-energy state is always associated with configuration (c), e.g., alternation of d_{x^2} and d_{y^2} in all Cartesian directions, thus forming a 3D checkerboard (the total energies of the single, columnar, and checkerboard OBS states are provided in Appendix A). In such a minimum-energy state, electrons occupy an orbital that is pointing to orthogonal directions between all nearest-neighbor transition elements, such as alternation of d_{xy}/d_{yz} orbitals for a material with a t_{2g} degeneracy, or alternation of d_{y^2}/d_{x^2} orbitals for a material with an e_g-level degeneracy as shown by our partial charge density maps of states near the Fermi level [Fig. 2, panels (a), (b), (d), and (e)]. This specific pattern is referred to as a G-type antiferro-orbital ordering [21,31,50] that minimizes orbital interactions between all nearest-neighbor TM sites on a perfectly cubic lattice. Significantly, these energy-lowering states all exhibit band gaps with respect to the cubic cell with equally occupied degenerate partners, even though no structural relaxation has been performed as yet (see Table I). We conclude here that in $LaVO_3$, $KFeF_3$, $KCoF_3$, $KCrF_3$, and $KCuF_3$, the electronic structure in the cubic cell distorts in order to remove the orbital degeneracy, thereby producing an antiferro-orbital arrangement and opening a band gap. These compounds therefore exhibit the signatures of a Jahn-Teller effect that is directly related to gapping.

2. When electronic delocalization of degenerate orbitals prevents the JTE

One might wonder at this stage why compounds with identical electronic degeneracy differ in their ability to have

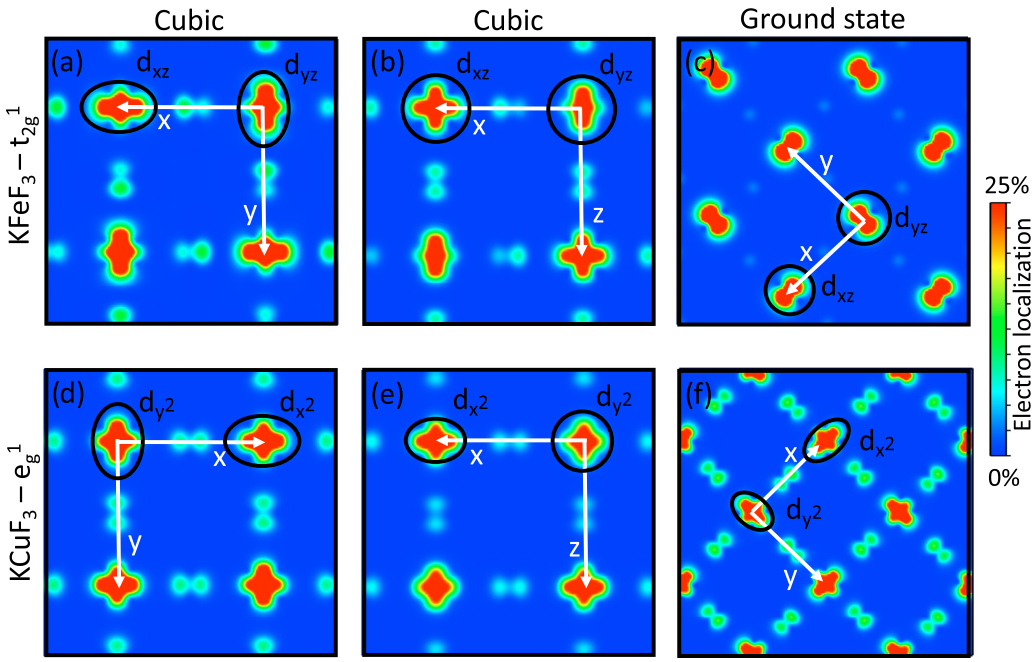

FIG. 2. Orbital orderings appearing in ABX_3 materials. Wave function squared maps of electrons located at the top of the valence bands (latest two occupied bands) for $KFeF_3$ [(a), (b), and (c)] and $KCuF_3$ [(d), (e), and (f)] in their unrelaxed cubic cells [(a), (b), (d), and (e)] and in the fully relaxed ground state structure [(c) and (f)].

a JTE. For example, $LaMnO_3$ does not exhibit a JTE whereas $KCrF_3$ does; similarly, $LaTiO_3$ has no JTE, whereas $KFeF_3$ does. To understand this, let us recall that the energy surface of a Jahn-Teller system, as expressed by Baraff *et al.* in Ref. [51], as a function of a displacement x can be represented as $E(x) = -F_{JT}x + \frac{1}{2}Kx^2$, consisting of a stabilizing electronic Jahn-Teller force F_{JT} associated with electronic degeneracy removal, and an opposing harmonic restoring force of the surrounding bond characterized by the force constant K—let us note that there might be other linear terms but this is out of the scope of the present paper. That the existence of degeneracy of partially filled states does not automatically force a Jahn-Teller distortion is clear from the competition between these two terms: if the relevant (degenerate) orbitals are too hybridized or delocalized (weak F_{JT}), or the harmonic response of the bonds about to be deformed is too stiff, degeneracy will not lead to a Jahn-Teller distortion. Strongly (weakly) *p-d* hybridized systems will tend to have a weaker (stronger) Jahn-Teller force. To assess such tendencies, one must carry out a Jahn-Teller distortion inspecting the total (electron-electron, electron-ion, and ion-ion) energy terms, not just orbital energies. This is readily done in DFT supercell theory.

To assess the difference in hybridization between fluorides and oxides, Fig. 3 shows the projected density of states of isoelectronic pairs ($LaTiO_3$ versus $KFeF_3$, as well as $LaMnO_3$ versus $KCrF_3$) in the high-symmetry cubic cell with equal occupancies of degenerate partners. As one can see, the fluorine-based compounds show minimal hybridizations between the *B-d* and *X-p* states, and the bandwidth associated with degenerate partners is rather narrow, thus resulting in a localized electronic structure and *d-d*-like band edges. On the other hand, for oxygen-based perovskites, the hybridization between *B-d* and *X-p* states and the bandwidth associated with degenerate partners increases continuously upon adding electrons to the *d* levels, until reaching a "charge transfer insulator" regime for $LaMnO_3$—i.e., an anion-*p*-like valence band maximum and cation-*d*-like conduction band minimum. This thus suggests that oxides have more delocalized *d* states than fluorides. Thus, in the oxides the Jahn-Teller force can be too weak and might be overcome by the restoring force but in the fluorides the Jahn-Teller force is stronger and might win. This is what we see in Table I.

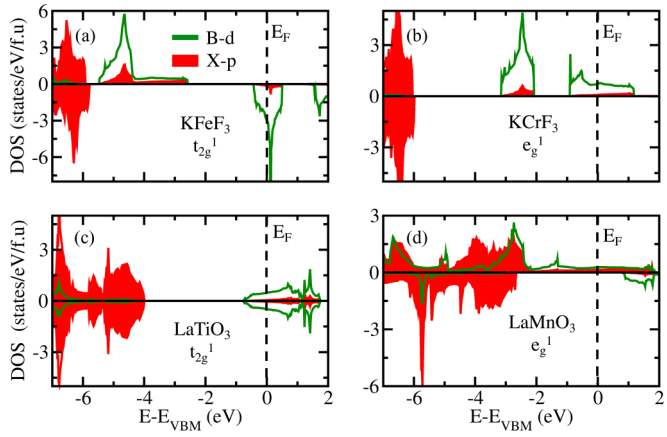

FIG. 3. Electronic structure of compounds with isoelectronic degeneracies. Projected density of states on *B-d* (green) and *X-p* (red) states in materials showing a t_{2g} [$KFeF_3$ and $LaTiO_3$, panels (a) and (c)] and e_g [$KCrF_3$ and $LaMnO_3$, panels (b) and (d)] isoelectronic degeneracies in their cubic cell. The vertical line indicates the Fermi level. A simple FM order is used.

To next check how the degree of localization of degenerate orbitals induces Jahn-Teller displacements, we design enhanced localization in $LaTiO_3$ by increasing the lattice constant, i.e., using a (negative) hydrostatic pressure. Starting from this new cubic cell in which the bandwidth of the t_{2g} degenerate partners is reduced by 0.5 eV with respect to the unperturbed cubic cell, we again nudge the Ti^{3+} electron to specific t_{2g} partners (see Appendix B). $LaTiO_3$ now develops a small electronic instability ($\Delta E_{\mathrm{OBS-no\,OBS}} = -6$ meV/f.u.) producing an antiferro-orbital occupancy between all nearest-neighbor Ti^{3+} sites and opening a band gap of 0.1 eV. Therefore, upon decreasing $B\,d$–$X\,p$ hybridizations and the t_{2g}-level bandwidth, $LaTiO_3$ undergoes a Jahn-Teller effect.

Finally, one may question the choice of the U value used in the present work. Using an enormous U value in DFT + U will always tilt the balance in favor of degeneracy removal. But this has to be judged on the basis of reasonableness of the choice of an arbitrary U. To this end we have used in the current work a rather low U value of 3.5 eV. Increasing for $LaTiO_3$ U to 5 eV can also result in a weak electronic instability but in fact, it is just associated with an increase of the cubic cell volume. However, such a large repulsion on Ti-3d levels was previously shown [34] to be totally irrelevant for studying $LaTiO_3$. In $LaMnO_3$ no electronic instability is found for any U (5 eV, 7.5 eV). This is likely due to the intrinsic charge transfer insulator nature of this compound (the valence band being oxygen like); increasing U has here the effect of pushing down in energy Mn-d levels and thus increasing anion p–Mn d hybridizations.

We conclude that delocalized degenerate states can prevent an electronic instability and the ensuing Jahn-Teller effect despite the presence of orbital degenerate states. This also explains why $SrVO_3$ and $CaVO_3$, showing strongly hybridized electronic structures, do not develop a JTE and thereby stay metallic in bulk.

3. *Trends in Jahn-Teller energies with orbital occupancy*

Although $LaVO_3$ exhibits $B\,d$–$X\,p$ hybridizations similarly to $LaTiO_3$, the former compound possesses a robust electronic instability in the cubic cell (an energy lowering of 297 meV; Table I), while $LaTiO_3$ has zero stabilization energy. This reflects the fact that the JT force is larger in systems with higher orbital occupancy—$LaVO_3$ with two electrons, $t^2_{2g\uparrow}$, relative to $LaTiO_3$ with just one, $t^1_{2g\uparrow}$. Similarly, the energy gain associated with breaking orbital degeneracies increases when going from t^1_{2g} in $KFeF_3$ to a t^2_{2g} in $KCoF_3$. In general, one expects that triply degenerate t_{2g} states occupied by 2 electrons will have greater Jahn-Teller instability than t_{2g} states occupied by 1 electron because of electron repulsion. Specifically, (i) for a single electron in a triply degenerate t_{2g} level there is no repulsion within that shell, so electron delocalization on all three levels is possible, weakening JT. On the other hand, (ii) if there are two electrons in t_{2g}, electron repulsion exists even if one places electrons in different degenerate partners, leading to a driving force for degeneracy removal. We next turn to study the trends in the deformation amplitudes.

B. The Q_2^- octahedral deformation mode is a Jahn-Teller distortion

1. *Electronically unstable cubic structures develop the Q_2^- octahedral deformation upon relaxation*

While the literature often ascribes Q_2^+ and Q_2^- modes to a JTE [2,12], we inspect here the type of distortion forced by the spontaneous electronic instability in the hypothetical cubic structure of $LaVO_3$, $KFeF_3$, $KCoF_3$, $KCrF_3$, and $KCuF_3$. To that end, we allow these systems to change their structures by fully developing energy-lowering displacements. Application of structural relaxation techniques (following quantum mechanical forces to zero force configurations) reveals that all these systems develop specifically the antiphase Q_2^- octahedral deformation that we therefore consider as the fingerprint of the JTE in these systems. We tested the Q_2^+ octahedral deformation mode but this octahedral deformation mode produces lower energy gains than the Q_2^- mode (see Appendix C).

Symmetry-adapted mode analysis of the relaxed DFT structures (starting from experimentally observed structures and magnetic orders) are presented in Table II. One can appreciate the development of the specific Q_2^- mode by the presence of a shifted single well potential energy surface associated with the Q_2^- mode starting from a cubic cell, signaling the presence of a Jahn-Teller force F_{JT} (see Appendix D). Note that the shifted single wells are independent of the spin order—FM and AFM orders yield similar results—and thus the magnetic order at low temperature may be a consequence of the specific orbital orderings forced by the electronic instability, but not its cause. The significance of the development of this specific Q_2^- mode [Fig. 1(d)] is that it is characterized by *opposite* octahedral deformations between nearest sites, and is thus able to accommodate and amplify the incipient orbital orderings [Figs. 2(c) and 2(f)]. Specifically, the B-X bonds expand and contract in the plane defined by the alternating directions of the occupied orbitals.

We emphasize that the appearance of an antiphase rotation propagating orthogonally to the Jahn-Teller distortion leads to very small additional components to the symmetry-allowed Jahn-Teller distortion in which O apices move inward or outward (Appendix E explains that the antiphase rotation and the Q_2^- motion displacement patterns describe orthogonal planes in $KCrF_3$ for minimizing electronic superexchange). Although it is sometimes proposed to come from additional electron interactions [52], it is just a consequence of the X_6 rotation (see Appendix F).

2. *Theory versus experimental observation for the Q_2^- octahedral deformation mode*

The predicted specific symmetry of the Q_2^- mode is precisely what is needed to explain the cubic to tetragonal I_4/mcm structural transition in $KCrF_3$ and $KCuF_3$ (observed at $T = 973$ K and 800 K [53,54], respectively), and of the $Pbnm$ to $P2_1/b$ structural transition observed in RVO_3 compounds (R = Lu-La, Y) [31,55]. Table II summarizes the calculated versus experimental values of the *amplitudes* of the Q_2^- displacements, showing very good agreement.

TABLE II. Amplitudes associated with structurally distorted octahedra in the ground state of ABX_3 perovskites. Amplitudes of distortions (in Å) associated with the Q_2^+ and Q_2^- modes (irreducible representations M_3^+ and R_3^-, respectively) distorting octahedra of the optimized structures starting from a cubic cell with the A cation located at the corner of the cell. Experimental values extracted from structures available in literature are provided in parentheses. The Goldschmidt t factor is also reported, as well as the magnetic state observed experimentally at low temperature and assumed in the simulation for the relaxation of the ground states.

	t factor	Magnetic order	Space group	Q_2^+ (M_3^+) Calculated (Expt.)	Q_2^- (R_3^-) Calculated (Expt.)
$LaTiO_3$	0.93	AFMG	$Pbnm$	0.040 (0.041 [56])	
$LaMnO_3$	0.94	AFMA	$Pbnm$	0.324 (0.357 [30])	
$LaVO_3$	0.95	AFMC	$P2_1/b$	0.005 (0.009 [57])	0.093 (0.079 [57])
			$Pbnm$	0.078 (0.090 [58])	
$KFeF_3$	1.00	AFMG	I_2/a		0.104 (–)
$KCoF_3$	1.01	AFMG	$P\bar{1}$		0.003 (–)
$KCrF_3$	0.99	AFMA	I_2/m		0.336 (0.316 [28])
			I_4/mcm		0.300 (0.299 [28])
$KCuF_3$	1.03	AFMA	I_4/mcm		0.335 (0.355 [29])

C. The Q_2^+ motion in $LaTiO_3$ and $LaMnO_3$ is a consequence of classic octahedral rotations and tilting, not a fingerprint of an electronic Jahn-Teller effect

Consistently with the absence of electronic instabilities in the high-symmetry $Pm\bar{3}m$ cubic cell of $LaTiO_3$ and $LaMnO_3$, we find that the Q_2^+ and Q_2^- octahedral deformations are associated with a single well energy potential [see Figs. 4(a) and 4(b)] and are unable to open a band gap. Such observations were already raised by Lee *et al.* for $LaMnO_3$ in Ref. [59]. This means that although a sizable Q_2^+ octahedral deformation mode appears in the ground state structure of $LaTiO_3$ and $LaMnO_3$, this mode is not produced by an electronic instability and does not lift orbital degeneracies or produce the metal-to-insulator transition, all being key aspects of the Jahn-Teller effect. Let us note that the amplitude of the Q_2 octahedral deformation modes reported in Table II are not really different between isoelectronic compounds such as

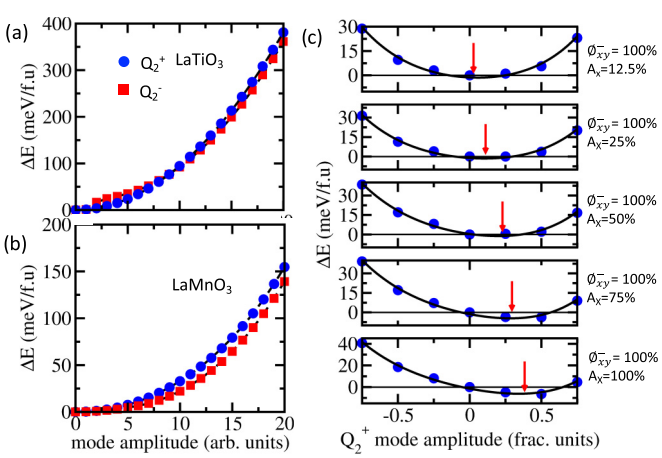

FIG. 4. Induced Q_2^+ motions through lattice mode couplings. (a) and (b) Energy versus Q_2^+ (filled blue circles) and Q_2^- (filled red squares) mode amplitudes (arbitrary units) in $LaTiO_3$ (a) and $LaMnO_3$ (b) using a FM order starting from a cubic cell. (c) Energy difference (in meV/f.u.) versus Q_2^+ mode amplitude at fixed amplitude of ϕ_{xy}^- and A_X in $LaMnO_3$ using a FM order. Here 1 (100%) represents the amplitude appearing in the ground state. The reference energy is set at 0 amplitude of the Q_2 modes.

$LaMnO_3$ and $KCrF_3$ (or $KCuF_3$), with the exception of their symmetry, suggesting that mass differences between F and O ions do not explain the different physical properties between fluorine and oxide compounds [60].

Nevertheless, these compounds develop two antiphase and one in-phase X_6 rotation (due to low-t factors; see Table II) that allow a specific lattice mode coupling between the Q_2^+ mode plus the antiphase rotation ϕ_{xy}^- and the antipolar motion A_X (sketched in Fig. 1 of Ref. [34]) of the form $F \propto \phi_{xy}^- A_X Q_2^+$ in the free-energy expansion as identified in Ref. [21]. The appearance of finite amplitudes of ϕ_{xy}^- and the A_X modes automatically forces finite amplitudes of the Q_2^+ mode in order to lower the total energy as we see in Fig. 4(c) for $LaMnO_3$. A similar result is found for $LaTiO_3$ (not shown). Although the dependence of the Q_2^+ mode on rotation amplitude in $LaMnO_3$ was already shown in Ref. [59], we show that the Q_2^+ is nothing but a consequence of ABX_3 distortions originating from pure steric atomic size effects captured already by the 1926 pre-quantum Goldschmidt tolerance factor [13]. In analogy with improper ferroelectrics [61,62], the Q_2^+ mode can be thought of as an improper mode, being a result of a specific octahedral rotation pattern: a combination of two antiphase and one in-phase rotation. In contrast to often articulated statements [3,5,30,56,63] this Q_2^+ motion should not be confused with a Jahn-Teller distortion originating from an electronic instability. The improper mode origin of Q_2^+ is consistent with previous theoretical reports of strong Q_2^+ mode amplitude in compounds that lack degenerate levels [22], clearly signaling that this mode cannot originate from an electronic instability.

1. The appearance of a Q_2^+ mode is not a statement of strong dynamical correlation effects

Leonov *et al.* [3] highlighted the importance of dynamical correlations in stabilization of the Q_2^+ mode in $LaMnO_3$. They plotted the potential energy surface as a function of the Q_2^+ mode amplitude with dynamical mean field theory (DMFT) simulations starting from a cell with rotations and the A_X mode, explaining that "in the calculation we change only the parameter ∂_{JT} (i.e., the amplitude of the Q_2^+ mode) … and keep the value of the MnO_6 octahedron tilting and rotation fixed." As can be seen by comparing our mean-field DFT

result of Fig. 4(c) with their DMFT results (Fig. 8 of Ref. [3]), the two agree closely, suggesting that in this case, adding dynamic electronic correlations does not bring any new features to the understanding of the octahedral deformation in ABX_3 materials.

2. *The origin of the improper Q_2^+ motion in* $LaMnO_3$

Our first-principles results demonstrate that the Q_2^+ mode is a simple consequence of octahedral rotations, but one wonders whether one can extract experimental evidence of this phenomena. At high temperature, $LaMnO_3$ adopts a rhombohedral $R\bar{3}c$ phase that is characterized by an antiphase rotation ϕ_{xyz}^- around all Cartesian axes and in which no octahedral deformation or related phenomena such as an orbital ordering are reported [30,64]. This is compatible with our models since (i) no electronic instability yielding a Q_2^- Jahn-Teller distortion mode is identified in $LaMnO_3$ and (ii) such X_6 octahedral tilt pattern does not allow A_X and Q_2^+ modes to develop by symmetry. Once $LaMnO_3$ transforms to the *Pbnm* cell around 750 K, one observes that experimental structures at various temperature taken from Ref. [30] develop an A_X distortion whose amplitude increases with decreasing temperature, while ϕ_{xy}^- is not temperature dependent. Upon increasing of the A_X mode amplitude on cooling, the Q_2^+ mode amplitude increases (see Appendix G for symmetry-adapted modes of these structures). This thus confirms the "improper appearance" of the Q_2^+ octahedral distortion mode.

3. *The origin of the orbital ordering in* $RTiO_3$ *(R = Lu-La, Y)*

Along with $LaMnO_3$, $LaTiO_3$ is often taken as a textbook example of compounds exhibiting a Jahn-Teller effect. Just as in Ref. [34], we again show here that $LaTiO_3$ exhibits a very weak improper Q_2^+ octahedral deformation mode. The single Ti-d electron is localized in an $\alpha d_{xy} + \beta d_{xz} + \gamma d_{yz}$ orbital whose α, β, γ coefficients depend on the sterically induced octahedral rotation, thus resulting in the various orbital orderings as a function of the rare-earth ionic radius (i.e., of the amplitude of the induced octahedral rotations) as demonstrated by some of the present authors in Ref. [34].

D. Competing Jahn-Teller effect and sterically induced Q_2^+ mode is at the core of the entangled spin-orbital properties in RVO_3 compounds

Although Q_2^+ and Q_2^- distortions have totally different origins, they can coexist as long as the Q_2^+ mode is allowed by symmetry. This is the case in $LaVO_3$ for which one observes finite amplitudes of the two modes in the low-temperature phase both at the theoretical and experimental levels (see Table II), although the Jahn-Teller distortion largely dominates. However, among the RVO_3 (R = Lu-La, Y) compounds, $LaVO_3$ shows the smallest octahedral rotations. One may question what happens for a compound showing larger X_6 rotations such as YVO_3.

Consistently with previous literature [21,55], full structural relaxation (atomic position + cell parameters) of YVO_3 yields a *Pbnm* ground state showing only the Q_2^+ mode at 0 K. Interestingly, through appearance of the Q_2^+ mode, a columnar orbital pattern is stabilized instead of the checkerboard pattern associated with the Jahn-Teller effect. Consequently, superexchange paths are enabled along the z axis thereby creating AFM interactions along the "columns." Such a behavior is indeed verified in our simulations: when starting from a $(\sqrt{2}a, \sqrt{2}a, 2a)$ cubic cell of YVO_3 with specific initial electron nudging (similar to those presented in Sec. III A), we find after variational self-consistency that the columnar orbital pattern is more stable than the checkerboard arrangement when considering the G-type AFM order ($\Delta E_{\text{che-col}} = +31$ meV/f.u.), and conversely for the C-type AFM order ($\Delta E_{\text{che-col}} = -74$ meV/f.u.). In other words, each Q_2 mode is associated with a specific orbital pattern, and consequently to a precise spin order.

Nevertheless, the checkerboard orbital pattern remains the global energy minimum in the cubic cell (between the G and C type AFM orders), a similar conclusion being drawn with a FM order ($\Delta E_{\text{che-col}} = -34$ meV). Therefore, YVO_3 should exhibit the signature of a Jahn-Teller effect although the low-T phase only shows the Q_2^+ mode. This is verified experimentally by the presence of an intermediate $P2_1/b$ symmetry characterized by the Q_2^- mode as shown by the symmetry-adapted mode analysis presented in Table I of Ref. [21]. Thus, the question is now, what is the driving force of the transition to the purely orthorhombic *Pbnm* cell at 0 K for YVO_3?

To get insights on this peculiar transition, we start from the high-symmetry $(\sqrt{2}a, \sqrt{2}a, 2a)$ cubic cell of YVO_3 and we freeze fixed amplitudes of all distortions appearing in the ground state structure except the Q_2^+ mode; i.e., we add only octahedral rotations and antipolar motions of ions. Then, we compute the potential energy surface associated with Q_2^+ or Q_2^- modes (see Fig. 5). Upon increasing "orthorhombic distortions," two antagonistic effects are observed irrespective

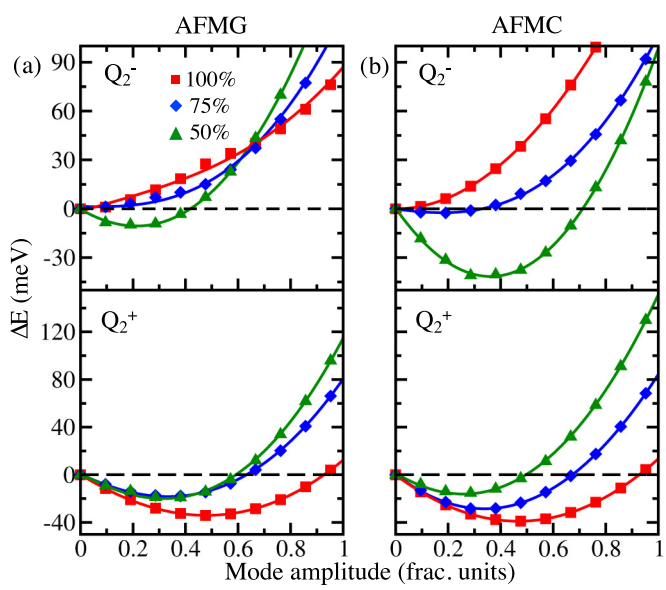

FIG. 5. Energy difference (in meV per 20-atom unit cell) as a function of the Q_2^+ and Q_2^- mode amplitudes (in fractional units) at fixed rotation and antipolar displacement amplitude (in %) appearing in the ground state structure of YVO_3 using the AFMG (a) and AFMC (b) order. The unit cell is fixed to a $(\sqrt{2}a, \sqrt{2}a, 2a)$ cell whose lattice parameter yields the ground state volume. Here 1 is actually the amplitude appearing in the ground state structure.

of the AFMG or AFMC magnetic order: (i) the Q_2^+ mode describes a single well potential whose energy minimum is progressively shifted to larger amplitudes while (ii) the Q_2^- mode vanishes. The former observation is in line with the improper origin of the Q_2^+ distortion discussed in Sec. III C but the latter finding indicates that orthorhombic distortions produce a crystal field sufficient to split the t_{2g}-level degeneracies [10] but also diminish electronic superexchange interaction at the core of the Jahn-Teller effect (see Appendix H).

Our results are closely compatible with the experimental phase diagram of rare-earth vanadates [31,55] and settle the issue that Q_2^- and Q_2^+ have totally different origins, the former being the signature of the Jahn-Teller effect while the latter is just a consequence of the ubiquitous octahedral rotations appearing in perovskites. RVO$_3$ are then unique materials in the sense that they are the only oxide perovskites with a B-3d element showing a Jahn-Teller effect plus the sterically induced Q_2^+ mode; thereby they are the only members possessing entangled spin-orbital properties associated with a JTE.

IV. CONCLUSIONS

We have explained the modalities enabling a Jahn-Teller effect in ABX_3 perovskites and identified its signature: strongly localized electronic states are the key factor for a spontaneous electronic instability to produce a Jahn-Teller distortion with a specific octahedral deformation pattern that is experimentally detectable and detected. In materials with larger anion-p and B-cation-d state hybridizations, there is no electronic instability that can break orbital degeneracies and the observed octahedral deformation has a distinct symmetry that is pushed by lattice mode couplings with rotations. The Q_2^+ octahedral deformation, appearing in LaMnO$_3$ or LaTiO$_3$, is not induced by an electronic instability and thus it is not a Jahn-Teller distortion. It is a consequence of octahedral rotations and tilts often appearing in the perovskite oxides due to pure semiclassical atomic size effects, i.e., geometric steric effects.

Our work provides a single theory explaining the Jahn-Teller effect and its specific signatures and reconciles the numerous experimental results of ABX_3 materials studied to date. Last but not least, our results settle the fact that dynamical correlations, and the Mott-Hubbard model, are absolutely not an essential aspect of the physics of ABX_3 materials showing insulating states despite the presence of degenerate states in the parent cubic cell, thereby defining DFT as a sufficient platform to study the physics of ABX_3 materials.

Some details of the method. DFT calculations are performed with the VASP package [43,44] and electrons are nudged using the modified VASP routine [45]. For exploration of orbital broken states using the HSE06 functional in cubic cells, a preconverged wave function is initially obtained using DFT + U with the orbital occupancy control routine and symmetry off for the wave function. Starting from this initial guess, we then perform HSE06 calculation allowing the solver to update orbital occupancies, still without symmetry of the wave function. We used PAW potentials with the outer 4s, 4p, and 3d B-cation electrons explicitly treated in the simulations. Since electronic instability is sensitive to the pressure, we determine the equilibrium volume of cubic cells. Full structural relaxation (lattice parameters plus cell internal coordinates)—reduced to lattice parameters for cubic cell relaxations—is performed until forces are lower than 0.5 meV/Å (increased to 0.01 meV/Å for cubic cell relaxations). We use a 6×6×4 (8×8×8) k-point mesh for the relaxation of the ($\sqrt{2}a$, $\sqrt{2}a$, $2a$) cubic cells (primitive cubic cells), and increase to 8×8×6 for plotting energy potential surfaces and seeking OBS, accompanied by an energy cutoff of 500 eV. Energy potential surfaces were plotted with symmetry of the wave function off, in order to allow electrons to occupy the lowest energy state.

ACKNOWLEDGMENTS

The work of J.V. has been supported by the European Research Council (ERC) Consolidator grant MINT under Contract No. 615759. Calculations took advantage of the Occigen machines through the DARI project EPOC A0020910084 and of the DECI resource FIONN in Ireland at ICHEC through the PRACE project FiPSCO. The work of A.Z. was supported by the Department of Energy, Office of Science, Basic Energy Science, MSE division, under Grant No. DE-FG02-13ER46959 to CU Boulder. J.V. acknowledges support from A. Ralph at ICHEC supercomputers.

APPENDIX A: TOTAL ENERGIES OF ORBITAL BROKEN SYMMETRY STATES IN CUBIC CELLS

We have performed total energy calculations starting from ($\sqrt{2}a$, $\sqrt{2}a$, $2a$) cubic cells and preconverged solutions in which electrons are nudged in specific degenerate partners, forming either (i) a single pattern with the same occupied orbital on all transition metal sites, (ii) a "columnar arrangement" with alternating orbitals in the xy plane (such as d_{x^2}/d_{y^2} for e_g degeneracies or d_{xz}/d_{yz} for t_{2g} degeneracies) with similar stackings along the z axis, or (iii) a "3D checkerboard pattern" with alternating orbital occupancies between nearest-neighbor transition metal sites. Results for KFeF$_3$, KCoF$_3$, KCrF$_3$, KCuF$_3$, and LaVO$_3$ are presented in Table III for GGA + U simulations.

APPENDIX B: DENSITY OF STATES OF LaTiO$_3$ UNDER NEGATIVE PRESSURE

In order to check the role of electron localization on the Jahn-Teller effect, we have compared the projected density of

TABLE III. Energy difference [in meV per ($\sqrt{2}a$, $\sqrt{2}a$, $2a$) cubic cell] between OBS states and equally occupied degenerate partner solutions for different initially imposed OBS states. A ferromagnetic order is used.

	$\Delta E_{\rm sin}$ (meV)	$\Delta E_{\rm col}$ (meV)	$\Delta E_{\rm check}$ (meV)
KFeF$_3$	−2513	−2583	−2621
KCoF$_3$	−2804	−2866	−2902
LaVO$_3$	−689	−1072	−1187
KCrF$_3$	−108	−490	−494
KCuF$_3$	−27	−277	−282

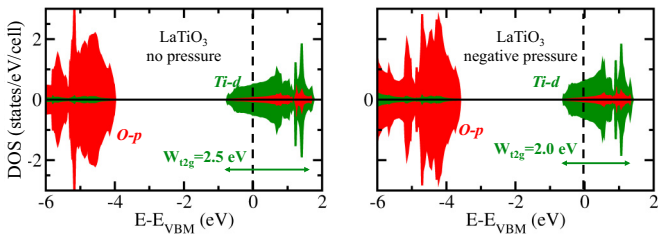

FIG. 6. Projected density of states on O-p levels (red area) and Ti-d levels (green area) in a cubic cell of $LaTiO_3$ without (left panel) and with a negative pressure (right panel).

states of $LaTiO_3$ with and without a negative pressure (i.e., a volume expansion). Under a volume expansion, $LaTiO_3$ still shows minimalistic hybridizations between O p–Ti d levels but the bandwidth W associated with t_{2g} levels is strongly reduced with respect to the unperturbed cubic cell (see Fig. 6). Following the reduction of the bandwidth, a narrow electronic instability able to break orbital degeneracies and to produce a G-type antiferro-orbital arrangement is observed ($\Delta E = -6$ meV/f.u.).

APPENDIX C: ENERGY GAIN ASSOCIATED WITH Q_2^+ AND Q_2^- OCTAHEDRAL DEFORMATION MODE

Starting from a high-symmetry ($\sqrt{2}a$, $\sqrt{2}a$, $2a$) cubic cell of the different compounds exhibiting a spontaneous electronic instability willing to break orbital degeneracies, we have nudged amplitudes of the Q_2^- (lowering the symmetry from $Pm\bar{3}m$ to I_4/mcm) or the Q_2^+ (lowering the symmetry from $Pm\bar{3}m$ to P_4/mbm) mode and we performed a full structural relaxation of lattice parameters and atomic positions using a FM order. Energy differences with respect to the perfectly cubic cell (in meV per 20-atom unit cell) for the two lattice modes are reported in Table IV for $LaVO_3$, $KFeF_3$, $KCoF_3$, $KCrF_3$, and $KCuF_3$. The Q_2^- lattice mode always produces the largest energy gain in these compounds, although Q_2^+ and Q_2^- are nearly metastable in $KCuF_3$ (note that the AFMA order slightly increases the energy stabilization of the Q_2^- mode by 2 meV/f.u. in $KCuF_3$).

TABLE IV. Energy gain (in meV) associated with the appearance of the Q_2^+ and Q_2^- octahedra mode deformation. Lattice parameters and atomic positions are relaxed. The reference energy is set to the cubic cell and a FM spin order was used.

	ΔE_{Q2+} (meV)	ΔE_{Q2-} (meV)
$KFeF_3$	−2739	−2760
$KCoF_3$	−2976	−3004
$LaVO_3$	−1153	−1325
$KCrF_3$	−1295	−1298
$KCuF_3$	−1019	−1020

APPENDIX D: POTENTIAL ENERGY SURFACES ASSOCIATED WITH Q_2^-

We report in Fig. 7 the energy gain associated with the condensation of the Q_2^- mode amplitude in a cubic cell (the 0 is set to the perfectly cubic cell) using a FM order. We

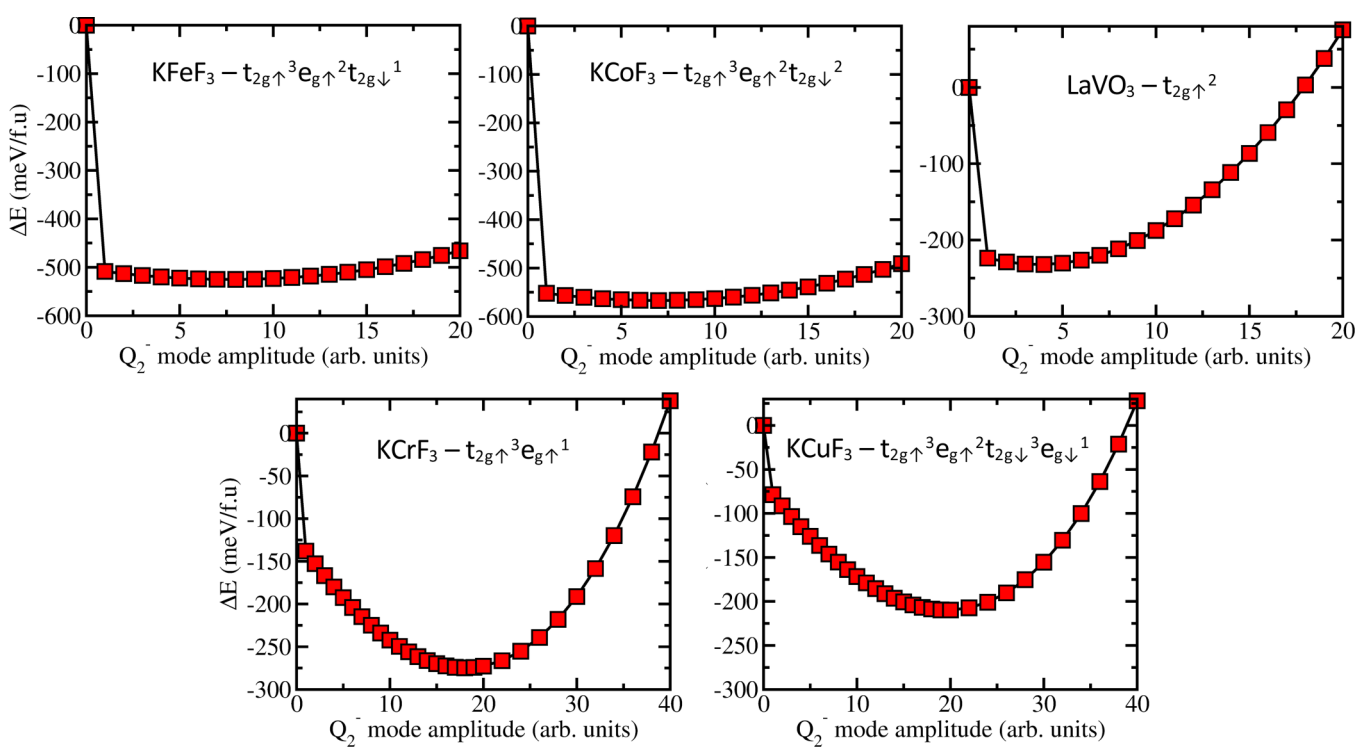

FIG. 7. Potential energy surfaces associated with the condensation of a Q_2^- octahedral deformation mode (arbitrary units) starting from a ($\sqrt{(2)}a$, $\sqrt{(2)}a$, $2a$) cubic cell for all materials exhibiting a spontaneous electronic instability willing to break orbital degeneracies. Potentials are plotted using a FM magnetic order.

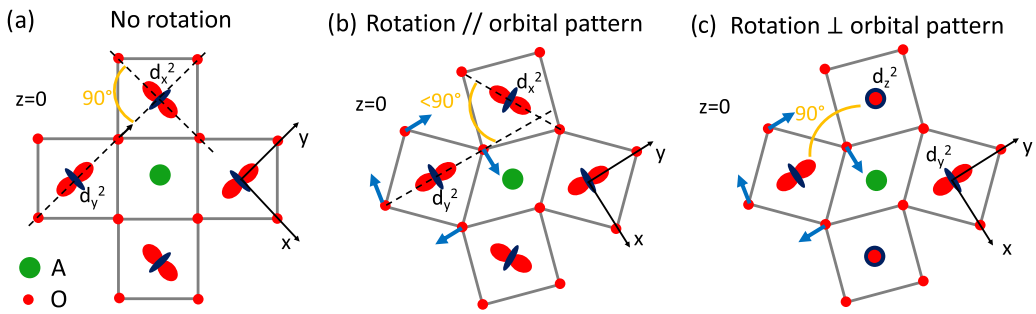

FIG. 8. Sketches of the interplay between orbital orderings and octahedra rotations. (a) A purely cubic cell without rotations. (b) and (c) Occupied orbitals and atomic displacements yielding rotations, displayed with blue arrows, are orthogonal (c) or coplanar (b).

note that in Fig. 7 no cell relaxation was performed and lattice parameters were fixed to the cubic cell, unlike the results reported in Table IV where full geometry relaxation was performed yielding a tetragonal cell. As one can see, $KFeF_3$, $KCoF_3$, $LaVO_3$, $KCrF_3$, and $KCuF_3$ are characterized by shifted single well energy potentials signaling the existence of a Jahn-Teller force F_{JT}, a signature of a JT effect.

APPENDIX E: THE ANTIPHASE ROTATION AND THE Q_2^- MOTION DISPLACEMENT PATTERNS DESCRIBE ORTHOGONAL PLANES IN $KCrF_3$ FOR MINIMIZING ELECTRONIC SUPEREXCHANGE

At low temperature, $KCrF_3$ shows a Jahn-Teller distortion (JTD) producing a F displacement pattern mostly along the x and z directions while the antiphase rotation produces F displacements along the x and y directions. Therefore, both motions produce displacements of ions in orthogonal planes, the xy and xz planes for the rotation and JTD, respectively. This situation is not fortuitous and it originates from electronic superexchange minimization. In the perfectly cubic cell, the Jahn-Teller effect produces a purely antiferro-orbital arrangement with orbital pointing along orthogonal directions between nearest-neighbor cation sites. This situation is sketched in Fig. 8(a) and it corresponds to the energy minimum of the electronic superexchange model, similarly to the Heisenberg model describing spin interactions (see chapter 6 of Ref. [2] for a detailed description of the Kugel-Khomskii model). Introducing a rotation producing atomic displacements coplanar with JTD atomic displacements, i.e., coplanar to the alternating orbital directions such as the situation sketched in Fig. 8(b), "orbitals directions" are not orthogonal anymore thereby weakening electronic superexchange. A rotation producing F displacements orthogonal to those described by the JTD [and so the alternating directions of orbitals such as the situation presented in Fig. 8(c)] preserves orthogonality between "orbital directions" and therefore the electronic superexchange is still minimized. We have checked this hypothesis in our simulations and we indeed observe that starting from a cubic cell in which we add the ground state rotation, the electronic instability associated with the situation presented in Fig. 8(c) is slightly larger than the situation presented in Fig. 8(b) by 6 meV/f.u. In conclusion, the antiphase rotation and the JTD propagate along orthogonal axes in $KCrF_3$ for the purpose of electronic superexchange minimization.

APPENDIX F: LOW-TEMPERATURE ORBITAL AND STRUCTURAL TRANSITION IN $KCrF_3$

In $KCrF_3$, the energy gain associated with the ϕ_z^- antiphase octahedral rotation is one order of magnitude smaller ($\Delta E_{rot} = -32$ meV/f.u.) than the energy gain produced by the electronic instability ($\Delta E = -124$ meV/f.u.), further amplified by the JT distortion ($\Delta E_{JTD} = -140$ meV/f.u.). Thus, the rotation appears at a temperature far below the JT effect. This is indeed observed experimentally: the material transits from a tetragonal to an I_2/m monoclinic cell at $T = 250$ K, a temperature much lower than that of the JT effect ($T = 973$ K). In the I_2/m symmetry, the octahedral rotation and the JT distortion have orthogonal atomic displacement patterns: X_6 groups rotate around the z axis—F motions along the x and y axes—while the JT distortion propagates along the y axis—F motions along the x and z axes. Such a peculiar orientation of propagation axes minimizes the electronic superexchange at the core of the JT effect (Appendix E) and enables by symmetry an extra component to the JT distortion in which X-apex anions move inward or outward the B cation, therefore very slightly modifying orbital shapes. However, unlike previous statements involving strong correlation effects, Slater superexchange, or covalent effects [52] for explaining the tetragonal to monoclinic transition, it is driven by nothing

TABLE V. Amplitudes (in Å) of distortions of $LaMnO_3$ for experimental structures refined at various temperatures. The high-symmetry cell is set to a cubic $Pm\bar{3}m$ cubic cell. The A cation is located at the corner of the cell. Irreps are provided in parentheses.

Temperature (K)	ϕ_{xy}^- (R_5^-)	ϕ_z^+ (M_2^+)	A_X (X_5^-)	Q_2^+ (M_3^+)
300	1.140	0.890	0.550	0.356
523	1.160	0.860	0.510	0.340
653	1.150	0.820	0.460	0.330
753	1.140	0.650	0.300	0.110
823	1.130	0.620	0.260	0.043
903	1.120	0.570	0.240	0.003
973	1.120	0.540	0.230	0.030

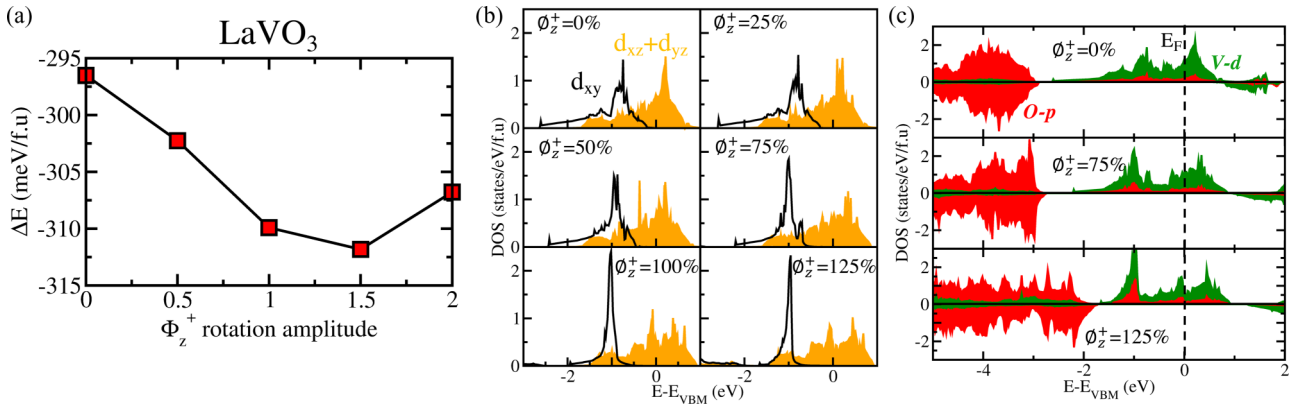

FIG. 9. Coupling between rotations and Jahn-Teller effect in $LaVO_3$. (a) Energy gain associated with breaking orbital degeneracies in $LaVO_3$ as a function of the in-phase rotation amplitude. Here 0 corresponds to the perfectly cubic cell. Only the in-phase rotation is added to the material. (b) Projected density of states on d_{xy} (black line) and d_{xz}/d_{yz} orbitals (orange area) in $LaVO_3$ for different amplitudes of in-phase octahedral rotations. (c) Projected density of states on V-d levels (in red) and O-p levels (in green) for different amplitudes of an in-phase octahedral rotation. A FM order is used in all these simulations.

other than a steric effect (a non magnetic (NM) simulation also provides a stabilization of the rotation mode). Let us note that the different orientations of occupied orbitals between the tetragonal (alternation of d_{x^2} and d_{y^2} orbitals) and monoclinic (alternation of d_{z^2} and d_{y^2} orbitals) cells simply originate from an arbitrary choice of different crystallographic parameters between the two symmetries.

APPENDIX G: SYMMETRY MODE ANALYSIS OF $LaMnO_3$ EXPERIMENTAL STRUCTURES

We have performed symmetry mode analysis of $LaMnO_3$ structures [30] extracted experimentally at different temperatures in order to get the amplitude associated with each individual distortion, most notably the antiphase ϕ_{xy}^- and in-phase ϕ_z^+ rotations, the antipolar A_X motion, and the Q_2^+ octahedral deformation. A high-symmetry cubic cell is set as the reference structure with A cations located at the corner. Results are presented in Table V.

APPENDIX H: COOPERATING AND COMPETING OCTAHEDRAL ROTATIONS AND JAHN-TELLER EFFECT IN $LaVO_3$

In the spirit of the electronic superexchange minimization analysis we have performed in $KCrF_3$ for explaining the interplay between the rotation and the JTD (Appendix E), we can perform such an analysis for $LaVO_3$. For the purpose of electronic superexchange minimization, the JTD prefers to share coplanar atomic displacements with the in-phase rotations since such situation preserves orthogonality of orbital directions between consecutive planes along the propagation axis of the distortion. Our first-principles simulations confirm this hypothesis and starting from a cell with either a single in-phase or antiphase rotation, we observe a slightly larger energy gain by breaking orbital degeneracies for the in-phase rotations than for the antiphase rotations ($\Delta E = -9$ meV/f.u. between the two solutions).

We nevertheless observe a surprising behavior with the amplitude of the in-phase rotation: the electronic instability breaking orbital degeneracies slightly increases upon increasing the rotation amplitude and then decreases for large rotation amplitude [Fig. 9(a)]. This observation is strictly compatible with the experimental phase diagram of RVO_3 compounds [31]: the JT effect temperature as a function of the tolerance factor (i.e., the rotation amplitude) follows the strength of our computed electronic instability as a function of the rotation amplitude. This *a priori* unexpected behavior has three origins: (i) The rotation amplitude first splits the degeneracy of the threefold-degenerate t_{2g} partners and the d_{xy} orbital is pushed to lower energies, leaving degenerate d_{xz}/d_{yz} orbitals at higher energies [see Fig. 9(b)]; note that at 0 amplitude of rotation, the point group symmetry is already reduced from O_h to D_{4h} by the DFT code due to the $(\sqrt{2}a, \sqrt{2}a, 2a)$ cubic cell we have used, and thereby t_{2g} levels are already split. (ii) Increasing rotations reduces the bandwidth of the degenerate partners [Fig. 9(b)], and *de facto* the strength of the electronic instability. (iii) But at large amplitude of rotations, O p–V d hybridization enters and decreases electron localization and the JTE strength [Fig. 9(c)].

[1] *The Jahn-Teller Effect: Fundamentals and Implications for Physics and Chemistry*, edited by H. Köppel, D. R. Yarkony, and H. Barentzen (Springer, Berlin, 2009).
[2] D. I. Khomskii, *Transition Metal Compounds* (Cambridge University Press, Cambridge, 2014).
[3] I. Leonov, D. Korotin, N. Binggeli, V. I. Anisimov, and D. Vollhardt, Phys. Rev. B **81**, 075109 (2010).
[4] H. Park, A. J. Millis, and C. A. Marianetti, Phys. Rev. Lett. **109**, 156402 (2012).
[5] E. Pavarini and E. Koch, Phys. Rev. Lett. **104**, 086402 (2010).
[6] I. Leonov, N. Binggeli, D. Korotin, V. I. Anisimov, N. Stojić, and D. Vollhardt, Phys. Rev. Lett. **101**, 096405 (2008).
[7] J. Varignon, M. Bibes, and A. Zunger, Phys. Rev. B **100**, 035119 (2019).

[8] G. Trimarchi, Z. Wang, and A. Zunger, Phys. Rev. B **97**, 035107 (2018).
[9] G. M. Dalpian, Q. Liu, J. Varignon, M. Bibes, and A. Zunger, Phys. Rev. B **98**, 075135 (2018).
[10] J. Varignon, M. Bibes, and A. Zunger, Nat. Commun. **10**, 1658 (2019).
[11] J. Varignon, M. N. Grisolia, J. Íñiguez, A. Barthélémy, and M. Bibes, npj Quantum Mater. **2**, 21 (2017).
[12] J. B. Goodenough, Annu. Rev. Mater. Sci. **28**, 1 (1998).
[13] V. M. Goldschmidt, Naturwissenschaften **14**, 477 (1926).
[14] Y. Tokura and N. Nagaosa, Science **288**, 462 (2000).
[15] H. A. Jahn and E. Teller, Proc. R. Soc. London, Ser. A **161**, 220 (1937).
[16] M. Baldini, V. V. Struzhkin, A. F. Goncharov, P. Postorino, and W. L. Mao, Phys. Rev. Lett. **106**, 066402 (2011).
[17] N. Binggeli and M. Altarelli, Phys. Rev. B **70**, 085117 (2004).
[18] K. I. Kugel and D. I. Khomskii, Zh. Eksp. Teor. Fiz. **64**, 1429 (1973).
[19] K. I. Kugel and D. I. Khomskii, Sov. Phys. Usp. **25**, 231 (1982).
[20] Y. Ren, T. T. M. Palstra, D. I. Khomskii, E. Pellegrin, A. A. Nugroho, A. A. Menovsky, and G. A. Sawatzky, Nature (London) **396**, 441 (1998).
[21] J. Varignon, N. C. Bristowe, E. Bousquet, and P. Ghosez, Sci. Rep. **5**, 15364 (2015).
[22] J. Varignon, N. C. Bristowe, and P. Ghosez, Phys. Rev. Lett. **116**, 057602 (2016).
[23] A. Stroppa, P. Barone, P. Jain, J. M. Perez-Mato, and S. Picozzi, Adv. Mater. **25**, 2284 (2013).
[24] A. Stroppa, P. Jain, P. Barone, M. Marsman, J. M. Perez-Mato, A. K. Cheetham, H. W. Kroto, and S. Picozzi, Angew. Chem., Int. Ed. **50**, 5847 (2011).
[25] J. Chaloupka and G. Khaliullin, Phys. Rev. Lett. **100**, 016404 (2008).
[26] D. Kumar, A. David, A. Fouchet, A. Pautrat, J. Varignon, C. U. Jung, U. Lüders, B. Domengès, O. Copie, P. Ghosez, and W. Prellier, Phys. Rev. B **99**, 224405 (2019).
[27] Y. Zhang, M. M. Schmitt, A. Mercy, J. Wang, and P. Ghosez, Phys. Rev. B **98**, 081108(R) (2018).
[28] S. Margadonna and G. Karotsis, J. Am. Chem. Soc. **128**, 16436 (2006).
[29] A. Okazaki and Y. Suemune, J. Phys. Soc. Jpn. **16**, 176 (1961).
[30] J. Rodriguez-Carvajal, M. Hennion, F. Moussa, and A. H. Moudden, Phys. Rev. B. **57**, R3189 (1998).
[31] M. H. Sage, G. R. Blake, C. Marquina, and T. T. M. Palstra, Phys. Rev. B **76**, 195102 (2007).
[32] Y. Yang, W. Ren, M. Stengel, X. H. Yan, and L. Bellaiche, Phys. Rev. Lett. **109**, 057602 (2012).
[33] E. Pavarini, E. Koch, and A. I. Lichtenstein, Phys. Rev. Lett. **101**, 266405 (2008).
[34] J. Varignon, M. N. Grisolia, D. Preziosi, P. Ghosez, and M. Bibes, Phys. Rev. B **96**, 235106 (2017).
[35] M. A. Carpenter and C. J. Howard, Acta Cryst. B **65**, 134 (2009).
[36] S. Xu, X. Shen, K. A. Hallman, R. F. Haglund, and S. T. Pantelides, Phys. Rev. B **95**, 125105 (2017).
[37] J. W. Furness, Y. Zhang, C. Lane, I. G. Buda, B. Barbiellini, R. S. Markiewicz, A. Bansil, and J. Sun, Commun. Phys. **1**, 11 (2018).
[38] C. Lane, J. W. Furness, I. G. Buda, Y. Zhang, R. S. Markiewicz, B. Barbiellini, J. Sun, and A. Bansil, Phys. Rev. B **98**, 125140 (2018).
[39] Q. Liu, Q. Yao, Z. A. Kelly, C. M. Pasco, T. M. McQueen, S. Lany, and A. Zunger, Phys. Rev. Lett. **121**, 186402 (2018).
[40] Q. Liu, G. M. Dalpian, and A. Zunger, Phys. Rev. Lett. **122**, 106403 (2019).
[41] J. M. Perez-Mato, D. Orobengoa, and M. I. Aroyo, Acta Cryst. A **66**, 558 (2010).
[42] D. Orobengoa, C. Capillas, I. Aroyo, and J. M. Perez, J. Appl. Cryst. **42**, 820 (2009).
[43] G. Kresse and J. Hafner, Phys. Rev. B **47**, 558 (1993).
[44] G. Kresse and J. Furthmüller, Comput. Mater. Sci. **6**, 15 (1996).
[45] J. P. Allen and G. W. Watson, Phys. Chem. Chem. Phys. **16**, 21016 (2014).
[46] J. P. Perdew, A. Ruzsinszky, G. I. Csonka, O. A. Vydrov, G. E. Scuseria, L. A. Constantin, X. Zhou, and K. Burke, Phys. Rev. Lett. **100**, 136406 (2008).
[47] S. L. Dudarev, S. Y. Savrasov, C. J. Humphreys, and A. P. Sutton, Phys. Rev. B **57**, 1505 (1998).
[48] J. Heyd, G. E. Scuseria, and M. Ernzerhof, J. Chem. Phys. **118**, 8207 (2003).
[49] A. V. Krukau, O. A. Vydrov, A. F. Izmaylov, and G. E. Scuseria, J. Chem. Phys. **125**, 224106 (2006).
[50] S. Miyasaka, J. Fujioka, M. Iwama, Y. Okimoto, and Y. Tokura, Phys. Rev. B **73**, 224436 (2006).
[51] G. A. Baraff, E. O. Kane, and M. Schlüter, Phys. Rev. B **21**, 5662 (1980).
[52] C. Autieri, E. Koch, and E. Pavarini, Phys. Rev. B **89**, 155109 (2014).
[53] S. Margadonna and G. Karotsis, J. Mater. Chem. **17**, 2013 (2007).
[54] L. Paolasini, R. Caciuffo, A. Sollier, P. Ghigna, and M. Altarelli, Phys. Rev. Lett. **88**, 106403 (2002).
[55] S. Miyasaka, Y. Okimoto, M. Iwama, and Y. Tokura, Phys. Rev. B **68**, 100406 (2003).
[56] M. Cwik, T. Lorenz, J. Baier, R. Müller, G. André, F. Bourée, F. Lichtenberg, A. Freimuth, R. Schmitz, E. Müller-Hartmann, and M. Braden, Phys. Rev. B **68**, 060401 (2003).
[57] P. Bordet, C. Chaillout, M. Marezio, Q. Huang, A. Santoro, S. W. Cheong, H. Takagi, C. S. Oglesby, and B. Batlogg, J. Solid State Chem. **106**, 253 (1993).
[58] H. Seim and H. Fjellvag, Acta Chem. Scand. **52**, 1096 (1998).
[59] J. H. Lee, K. T. Delaney, E. Bousquet, N. A. Spaldin, and K. M. Rabe, Phys. Rev. B **88**, 174426 (2013).
[60] B. Halperin and R. Engelman, Phys. Rev. B **3**, 1698 (1971).
[61] C. J. Fennie and K. M. Rabe, Phys. Rev. B **72**, 100103(R) (2005).
[62] E. Bousquet, M. Dawber, N. Stucki, C. Lichtensteiger, P. Hermet, S. Gariglio, J. M. Triscone, and P. Ghosez, Nature (London) **452**, 732 (2008).
[63] J. Hemberger, H. Krug von Nidda, V. Fritsch, J. Deisenhofer, S. Lobina, T. Rudolf, and P. Lunkenheimer, Phys. Rev. Lett. **91**, 066403 (2003).
[64] X. Qiu, T. Proffen, J. F. Mitchell, and S. J. L. Billinge, Phys. Rev. Lett. **94**, 177203 (2005).